
Article:
Feng, Chaobo, Lu, Bing-Qiang, Fan, Yunshan et al. (11 more authors) (2024) Amorphous 1-D nanowires of calcium phosphate/pyrophosphate:A demonstration of oriented self-growth of amorphous minerals. JOURNAL OF COLLOID AND INTERFACE SCIENCE. pp. 960-970. ISSN 0021-9797

https://doi.org/10.1016/j.jcis.2023.12.002

Amorphous 1-D nanowires of calcium phosphate/pyrophosphate: a demonstration of oriented self-growth of amorphous minerals

Chaobo Feng[+][a], Bing-Qiang Lu[+*][a], Yunshan Fan[a], Haijian Ni[a], Yunfei Zhao[a], Shuo Tan[a], Zhi Zhou[a], Lijia Liu[b], Jordan A. Hachtel[c], Demie Kepaptsoglou[d], Baohu Wu[e], Denis Gebauer[f], Shisheng He[*][a], Feng Chen[*][a,g]

Affiliations

[a]: Center for Orthopedic Science and Translational Medicine, Department of Orthopedic, Spinal Pain Research Institute, Shanghai Tenth People's Hospital, School of Medicine, Tongji University, Shanghai, 200072, P. R. China.

[b]: Department of Chemistry, University of Western Ontario, London, ON, N6A5B7, Canada.

[c]: Center for Nanophase Materials Sciences, Oak Ridge National Laboratory, Oak Ridge, Tennessee 37831, United States

[d]: SuperSTEM Laboratory, SciTech Daresbury Campus, Daresbury, WA4 4AD UK; Department of Physics, University of York, York, YO10 5DD UK

[e]: Forschungszentrum Jülich GmbH, JCNS-4, JCNS at MLZ, Lichtenbergstr. 1, 85748 Garching, Germany

[f]: Institute of Inorganic Chemistry, Leibniz University Hannover, Callinstr. 9, D-30167 Hanover, Germany.

[g]: Shanghai Key Laboratory of Craniomaxillofacial Development and Diseases, Stomatological Hospital and School of Stomatology, Fudan University, Shanghai, 200001 P. R. China.

[+]: These authors contributed equally.

Corresponding Authors

*E-mail: bqlu@tongji.edu.cn; tjhss7418@tongji.edu.cn; fchen@tongji.edu.cn.

Abstract

Amorphous inorganic solids are traditionally isotropic, thus, it is believed that they only grow in a non-preferential way without the assistance of regulators, leading to the morphologies of nanospheres or irregular aggregates of nanoparticles. However, in the presence of (ortho)phosphate (Pi) and pyrophosphate ions (PPi) which have synergistic roles in biomineralization, the highly elongated amorphous nanowires (denoted ACPPNs) form in a regulator-free aqueous solution (without templates, additives, organics, etc). Based on thorough characterization and tracking of the formation process (e.g., Cryo-TEM, spherical aberration correction high resolution TEM, solid state NMR, high energy resolution monochromated STEM-EELS), the microstructure and its preferential growth behavior are elucidated. In ACPPNs, amorphous calcium orthophosphate and amorphous calcium pyrophosphate are distributed at separated but close sites. The ACPPNs grow via either the preferential attachment of ~2 nm nanoclusters in a 1-dimension way, or the transformation of bigger nanoparticles, indicating an inherent driving force-governed process. We propose that the anisotropy of ACPPNs microstructure, which is corroborated experimentally, causes their oriented growth. This study proves that, unlike the conventional view, amorphous minerals can form via oriented growth without external regulation, demonstrating a novel insight into the structures and growth behaviors of amorphous minerals.

Keywords

Amorphous inorganic solids; nanowires; calcium phosphate; calcium pyrophosphate; oriented growth.

1. Introduction

As an important inorganic mineral, calcium phosphate is abundant in nature and many organisms. For example, human bone is composed of 70% inorganic mineral (mainly apatite) and 30% organic matrix (mainly collagen), while tooth enamel is 97% hydroxyapatite, 1.5% proteins, and 1.5% water [1-4]. Among the diverse calcium phosphates members, calcium orthophosphates (CaPi, where Pi stands for the orthophosphate ion) play the major roles in hard tissue formation or biomedical applications [5]. They include the amorphous form (amorphous calcium phosphate, ACaPi), and crystalline ones such as hydroxyapatite, octacalcium phosphate, brushite, monetite, and (α, β) tricalcium phosphates. In comparison, calcium pyrophosphate (CaPPi, where PPi stands for the pyrophosphate ion), has been much less discussed regardless of its crystalline or amorphous (ACaPPi) forms. CaPPi crystals are normally observed in pathological tissues, especially in cardiovascular and articular cartilage [6-9]. Moreover, these ectopic calcifications are mostly composed of both CaPPi and CaPi crystals [10-14]. In the process of bone formation, PPi, which is mainly produced by hydrolyzing the phosphodiester bond in nucleotide triphosphates [15-17], acts as a critical regulator in the formation of CaPi [18-24], since they can effectively inhibit nucleation and crystallization of CaPi by antagonizing the binding of calcium with phosphate [20-21, 25]. It is believed that Pi and PPi synergistically control bone mineralization [24, 26-29].

The growth behaviors of biominerals, which govern the specific construction of the resulting materials (including the biomineralized tissues), have been one of the central topics in the field of biomineralization[30]. It has been established that substances prefer to grow into the shapes with minimum surface free energy from the perspective of thermodynamic equilibrium, which is typically described by the Gibbs–Curie–Wulff Theorem [31-33]. Thus, the crystals, due to the energy differences between their different facets (based on the microstructure of long-range order), favor the growth with certain spatial preferences [32, 34]. This thereby leads to corresponding facets exposed on the surface of crystals, forming distinct planes, angles, and edges [32, 35-38]. On the contrary,

in amorphous solids, as the atoms and ions are extremely disordered, or only ordered within a very short range, they are isotropic when viewing them in the size scale of nanometers or longer [37, 39]. Therefore, there is usually no energetic driving force for amorphous minerals towards a spatially preferential growth in the absence of external regulators (templates, additives, electrical field, magnetic field, etc), resulting in the morphologies of round nanospheres or irregular nanoparticles which have the lowest specific surface area [40-44]. Indeed, while a few previous amorphous nanowires of inorganic solids exhibited a preferential growth for their formation, the inductive contributions by the applied organics, templates, and electric field can not be ruled out [45-50]. Those conclusions are particularly applicable to ACaPi and AcaPPi [51-52].

However, in this work, we find a 1-D oriented growth behavior of an amorphous solid (Schematic 1). Inspired by the fact that Pi and PPi co-exist in the bodily fluids and interact with each other especially during biomineralization, we studied calcium phosphate formation in solutions including both of the ions. Surprisingly, we obtained nanowires of amorphous phase with high aspect ratio. The nanowires are composed of ACaPi and ACaPPi and their formation involves the assembly of nanoclusters or transformation of nanoparticles in a 1-D oriented fashion. The amorphous nanowires (denoted amorphous calcium phosphate-pyrophosphate nanowires, ACPPN) thus provide a novel perspective on structures and growth behaviors of amorphous minerals.

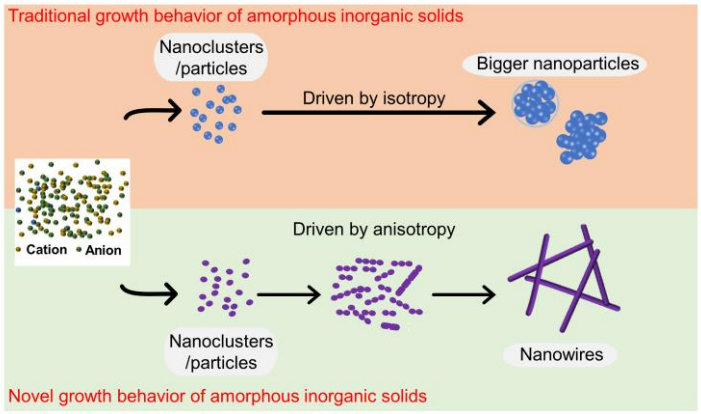

Schematic 1. Illustration of the key finding of this work: amorphous inorganic solids can grow in a 1-D oriented way without external regulators, demonstrating a novel anisotropy-driven growth behavior.

2. Results and Discussion

2.1 Preparation of ACPPNs

ACPPNs prepared at high atomic ratio of Ca/P (>0.05) without additives

ACPPNs are prepared by simply mixing the solutions of calcium source (Ca^{2+}) and phosphorus source (Pi and PPi, denoted as P_e), where the amount of Ca^{2+} is fixed at 1.00 mmol, but that of P_e is varied.

At first, high atomic ratio of Ca/P (>0.05; *i.e.*, amount of P_e <20 mmol) is applied and a two-step procedure is involved for ACPPNs formation. Typically, for an atomic ratio of Ca/P = 0.1 with 15% of P_e in the form of PPi (the remaining 85% in the form of Pi), we have obtained ACPPNs by adding 10.0 mmol P_e in two steps, that is, 5.0 mmol by 5.0 mmol sequentially. The two-step procedure facilitates the control over the pH of the reaction solution. As shown in Fig. 1a, nanowires with average diameters of 2.8 nm (n = 100) and lengths of up to hundreds of nanometers are formed, although thicker ones (e.g., diameters >10 nm) are also observed. Besides, nanoparticles with irregular shapes are obtained as well. In cryogenic transmission electron microscopy (Cryo-TEM) micrographs of the sample in the reaction solution, we also observe the nanowires, proving that this morphology is formed in the solution, rather than during the subsequent sample preparation (Fig. 1b). The electron diffraction (ED) pattern (inset of Fig. 1a) of the area with nanowires (labeled by dashed circle) exhibits no distinct reflections, indicating the amorphous character of the product, which is also confirmed by spherical aberration correction high resolution TEM (HR-TEM, Fig. 1c) and X-ray diffraction (XRD, inset of Fig. 1c). As we introduced above, nanowire morphology of ACaPi or ACaPPi has never been obtained before without external regulations such as additives, templating, etc., and is not seen in other amorphous inorganic materials either, to the best of our knowledge. Theoretically, when the diameter of nanowire is too thin, organic additives are required to stabilize the shape especially the ones with highly

disordered microstructure[53-57]. In comparison, ACPPNs in this work are additive-free nanowires.

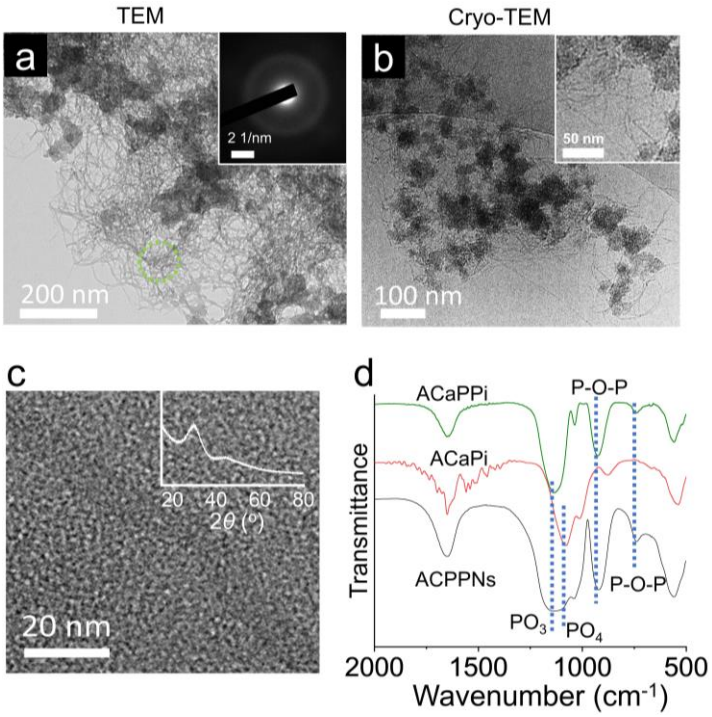

Fig. 1. Characterization of ACPPNs prepared at Ca/P = 0.1. (a) TEM micrograph and ED pattern of the area marked with a dashed green circle. (b) Cryo-TEM micrograph of the sample in the reaction solution with magnified local area in the inset. (c) Spherical aberration correction HR-TEM image at a temperature of -180 °C (created by liquid nitrogen) and XRD pattern (inset, two broad bumps at 2θ=~30 and ~45°) of the ACPPNs. No visible beam damage on the sample was observed after ED pattern capture. (d) FTIR spectra with dashed blue line labeling characteristic bands of specific groups as indicated. The assignment of the vibration modes follows the references [58-59].

X-ray photoelectron Spectroscopy (XPS) (Fig. S1a) and Energy dispersive spectroscopy (EDS) (Fig. S1b) prove the existence of Ca and P elements. Fourier transform infrared spectroscopy (FTIR) further verify the presence of PPi ($P_2O_7^{4-}$) in the ACPPNs due to the asymmetric vibrational bands of P-O-P at wavenumbers of 918 and 739 cm^{-1} and that of PO_3 at 1146 cm^{-1}, which is consistent with $P_2O_7^{4-}$ in ACaPPi (Fig. 1d). The presence of Pi (PO_4^{3-} or HPO_4^{2-}) is also confirmed by the asymmetric

stretching frequency of PO_4 at 1097 cm^{-1}, agreeing with the bands of $(H)PO_4$ in ACaPi as well (Fig. 1d). In comparison, when adding the same amount of P_e simultaneously in one step (rather than in two steps as above), more nanoparticles and fewer nanowires are formed, confirming that the two-step procedure is favorable for the formation of nanowires (Fig. S2). Also, importantly, the ACPPNs can keep the nanowire morphology after being stored at 37 °C even for 8 weeks without drying (Fig. S3).

To investigate the effect of Pi/PPi ratio on the morphology of ACPPNs, we varied the P_e percentages of PPi (0, 5, 10, 15, 25, 100%; other conditions are kept the same as above). For 0 % PPi, *i.e.*, only Pi as the P_e, a flake-shaped product is obtained and no nanowires are observed (Fig. S4a). From 5% (Fig. S4b), 10% (Fig. S4c), 15% (Fig. S4d), to 25% (Fig. S4e), the proportion of nanowires increases. For 100% PPi (Fig. S4f), *i.e.*, only PPi as the P_e, the TEM micrograph presents a typical irregular nanosphere morphology of amorphous calcium pyrophosphate [60]. Therefore, nanowires only form in a certain ratio range of Pi/PPi in the P_e.

The initial Ca/P atomic ratio also has an influence on the morphology of the products. When the initial Ca/P increases from 0.1 (Fig. 1) to 1.0, *i.e.*, 1.00 mmol P_e is used (other parameters are not changed), nanowires are still formed in the above-described two-step procedure (Fig. S5a). However, only very few nanowires are visible when Ca/P=2.0 (Fig. S5b), and no nanowires are observed when Ca/P=5.0 (Fig. S5c). FTIR spectra of these three samples show that Pi/PPi ratios in the products are significantly higher (Fig. S5d) comparing to that prepared with Ca/P=0.1 (Fig. 1d). We also investigated the effects of pH on the structure of the products. Based on a solution of pH=8 as discussed above, we compared the changes of morphology at different pH values. Under weakly acidic conditions (pH=6) (Fig. S6a), still the nanowires form, but they become much fewer under weakly basic conditions at pH=10 (Fig. S6b).

ACPPNs prepared at high atomic ratio of Ca/P (>0.05) with additives

Anionic polyelectrolytes with abundant carboxylate groups, such as polymaleic

acid (PMA) and sodium polyacrylate (PAA), are normally used to mimic non-collagenous proteins when studying biomineralization (e.g., inhibitor effects of nucleation and crystallization)[61], which are also typical additives for the preparation of ACP nanospheres[62]. However, the introduction of PMA and PAA into the ACPPNs formation system significantly increases the ratio of nanowires in the sample and even results in nearly pure nanowires. As shown in Fig. 2, in the presence of either PMA (Fig. 2a) or PAA (Fig. 2b), nanowires with average diameters of 2.8 (n = 100, although thicker ones with diameters >10 nm are also observed), and lengths of up to hundreds of nanometers are prevalent in the products, while nanoparticles are hardly visible by TEM observation. The predominance of nanowires in the products may be attributed to an inhibitory effect of PMA and PAA against nucleation and subsequent solid growth, as precipitation occurs much later than in the absence of PMA and PAA (~5 min vs. 0 min). We verified the amorphous phase by ED and XRD patterns (insets of Fig. 2a and 2b, Fig. S7), and the presence of Ca and P elements by XPS (Fig. S8). In the FTIR spectra (Fig. 2c), apart from the presence of Pi and PPi corresponding to the same bands as Fig. 1d, the existence of polymer is also proved by the stretching frequency of the carboxy ion (COO^-) at 1409 cm^{-1} (Fig. 2c).

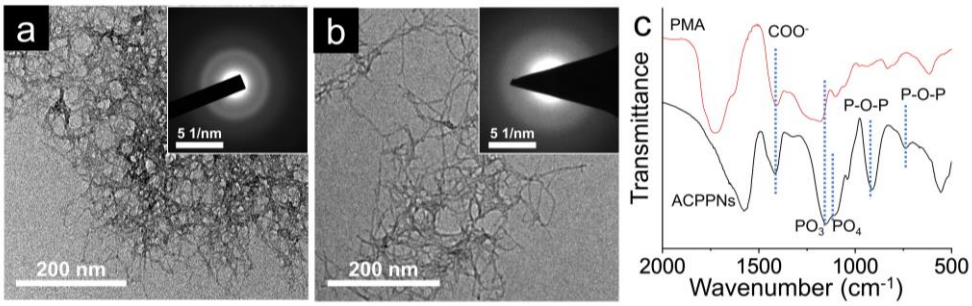

Fig. 2. Characterization of ACPPNs prepared at Ca/P = 0.1 in the presence of additives. (a, b) TEM images of ACPPNs prepared in the presence of PMA (a) or PAA (b). (c) FTIR spectra of ACPPNs prepared with PMA.

ACPPNs prepared at low atomic ratio of Ca/P (≤0.05)

We further decreased the atomic ratio of Ca/P to ≤0.05 (amount of P_e ≥20 mmol, without additives) to investigate nanowire formation in a one-step procedure. Given that the amount of P_e is much higher than that of Ca, the influence of precipitation on pH is minimal due to the buffer effect of the excess P_e, and therefore, it is not necessary to adjust the pH during the reaction as above. Hence, the one-step method can be used in this case. Here, the total P_e content is increased to 20.0 (Ca/P=0.050) and 40.0 mmol (Ca/P=0.025), while maintaining the proportion of PPi the same as above. It is found that the fraction of nanowires increases significantly (Fig. 3). Typically, when the Ca/P=0.025, nearly pure nanowires with a width of 3.0 ± 0.7 nm (n = 100, single nanowire or the ones at the edge of aggregates are used for measurements) and lengths of up to tens of nanometers are formed (Fig. 3b). The elemental map recorded by EDS confirms the presence of elements P and Ca (Fig. S9). With such a high P_e concentration, the stepwise addition of P_e seems to have little (or even adverse) influence on the product morphology (Fig. S10). Again, ED and XRD patterns confirm the amorphous phase (insets of Fig. 3a and b, Fig. S11). The FTIR spectra in Fig. 3c show that the intensity ratio of bands at 1146 cm^{-1} (PO_3 stretching) and 1097 cm^{-1} stretching (PO_4) is significantly higher than that in Fig. 1d, indicating the increase of PPi percentage in P_e, which is also confirmed by nuclear magnetic resonance (NMR) measurement as discussed in the following.

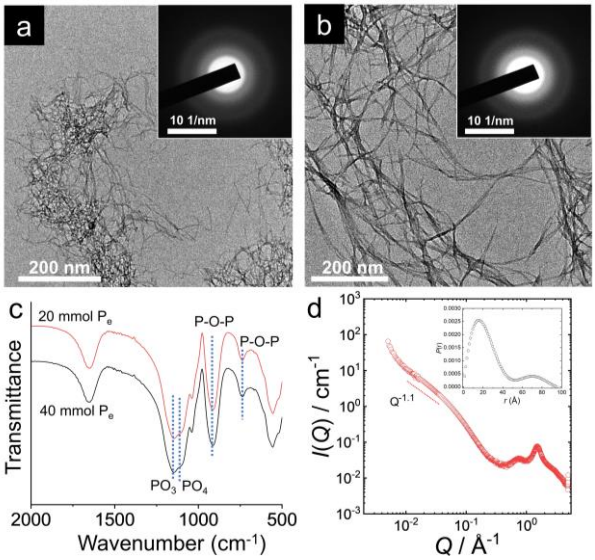

Fig. 3. Characterization of ACPPNs prepared at the atomic ratio of Ca/P ≤0.050 via a

one-step procedure. (a, b) TEM images of the ACPPNs prepared when the Ca/P is at 0.050 (P_e content 20.0 mmol) (a) and 0.025 (P_e content 40.0 mmol) (b). (c) FTIR spectra of the ACPPNs with dashed blue line labeling characteristic bands of specific groups as indicated. (d) One-dimensional integrated SAXS/WAXS profiles of the ACPPNs (Ca/P=0.025) dispersed in ethanol. The inset of (d) shows the pair distribution function $P(r)$ obtained from the SAXS scattering curve. Q: scattering vector.

The morphology and phase of the nanowires are also confirmed with small-angle X-ray scattering (SAXS) and wide-angle X-ray scattering (WAXS) (denoted as SAXS/WAXS). As shown in Fig. 3d, within the scattering vector (Q) range spanning from 0.009 $Å^{-1}$ to 0.5 $Å^{-1}$, the scattering patterns predominantly stem from nanowires, which is consistent with the TEM observation. The scattering curves exhibit Q^{-1} type scattering at lower Q values, indicating that the scatterers are largely constituted of flexible nanowires. Within the inset of Fig. 3d, the pair distribution function ($p(r)$) illustrates two distinct maxima within 0-50 Å and 50-100 Å, where the initial maxima is associated with the nanowire's diameter, and the latter one corresponds to their aggregations. Regarding the WAXS segment (Q > 0.5 $Å^{-1}$), the findings indicate that the nanowires dispersed in ethanol do not exhibit any crystal formation.

ACPPNs prepared with Pi and PPi added in separate steps

The observations above beg the question whether the pre-synthesized ACaPi and ACaPPi can transform into ACPPNs? In order to explore this further, we added Pi and PPi sequentially in two steps with a time interval of 3 s (Ca/P=0.1, P_e is 10.0 mmol, in which Pi and PPi are 8.50 and 0.75 mmol), by which ACaPi or ACaPPi was initially formed by the first added Pi or PPi, then further reacted with the next added PPi or Pi. Like above, nanowires are generated in the presence of both Pi and PPi although they are added in separate steps (Fig. S12a-b). Moreover, there are many more nanowires (Fig. S12a) when the PPi is added in the first step and Pi in the second (denoted as PPi-

and-Pi), than in the case of the reverse sequence of P_e addition (Pi-and-PPi) (Fig. S12b). It should be noted that when PPi or Pi is first added, pure ACaPPi or ACaPi forms primarily, and the next addition of Pi or PPi can only partially substitute PPi or Pi in the products. Furthermore, we extended the time interval between PPi and Pi addition and removed the excess P_e source during the interval by washing the precipitates at the first addition with a large amount of H_2O to avoid effects of the first-added excessive P_e. Again, nanowires form with PPi added in the first step (PPi-and-Pi, Fig. S12c), but they are nearly invisible with P_e added in reverse sequence (only crystalline CaPi, Fig. S12d). All of the above reveals that ACaPPi or ACaPi can transform into ACPPNs although their performance varies under different conditions. In essence, as discussed above, the nanowire mainly consists of ACaPPi rather than ACaPi, but only the addition sequence of PPi-and-Pi yields nearly pure nanowires (Fig. S12c). This further confirms that, (1) in addition to PPi, Pi is indeed included in nanowires as well; (2) excludes the possibility that PPi acts as the surfactant to induce the nanowire formation because PPi has been consumed in the first step of addition in the PPi-and-Pi sequence.

2.2 Microstructure of ACPPNs

We analyzed the typical products by solid state NMR spectroscopy (Fig. 4). The single pulse ^{31}P MAS NMR spectra show two resonances with chemical shifts of ~2.6 ppm and ~-6.5 ppm, which can be assigned to Pi (PO_4^{3-} or HPO_4^{2-}) and PPi ($P_2O_7^{4-}$) groups, respectively (Fig. 4a) [63]. The molar ratio (P_{ratio}) of P_e in Pi and PPi for the samples is calculated by integrating the corresponding Guassian peaks after deconvolution as shown in Fig. 4a. Based on the P_{ratio} value and TEM results, it can be inferred that the increase of the fraction of nanowires is associated with the higher PPi content in the products, indicating that the formed nanoparticles consist of more Pi while the nanowires contain more PPi. In the case of uniform nanowires, the P_{ratio} remains ~1:3 regardless of different synthesis procedures (one using PMA, and the other one at Ca/P=0.025 without additives).

Subsequently, we measured the ACPPNs prepared at Ca/P=0.025 via 2D solid state nuclear magnetic resonance (Fig. 4b-e). In the 2D ^{1}H-^{31}P HETCOR CPMAS NMR spectra (Fig. 4b), both Pi and PPi are strongly correlated with H. We further extracted the cross-section spectra at the ^{31}P chemical shift of Pi and PPi as indicated in Fig. 4c. They show that the PPi peak correlates with the resonance of H from adsorbed/structural H_2O while that of the Pi peak correlates with H of both H_2O and HPO_4^{2-}. This reveals that a certain fraction of phosphates is protonated to yield HPO_4^{2-}, but pyrophosphates are not. As the Ca/P molar ratio determined by ICP-OES analysis is 0.98, *i.e.*, very close to 1, we conclude that nearly all of the Pi are protonated in this sample. So, with these results and TG measurement (Fig. S13), the chemical formula of the nanowire is estimated to be $CaHPO_4 \cdot (Ca_2P_2O_7)_{1.5} \cdot xH_2O$ (the content of H_2O is flexible depending on the drying conditions).

Further insight into the relationship of Pi and PPi is obtained by ^{31}P-^{31}P NOESY CPMAS NMR spectra (Fig. 4d, e). At a mixing time of 6 s, no exchanges between the P_e from Pi and PPi are observed (Fig. 4d). However, when extending the mixing time to 12 s, which is still very short, exchanges (positive) peaks are clearly observed (Fig. 4e). This result shows that Pi and PPi are separately distributed at independent sites, but stay very close to each other. This anisotropy can be corroborated by STEM-EELS as well: data obtained on a short rod (Fig. 5, S14) indicates fundamental changes in the coordination of P_e within inner and outer spaces of ACPPNs, which is consistent with the spectra of ACaPi and ACaPPi, and thus agree with the anisotropic distribution of Pi and PPi. Therefore, we propose the structural model of ACPPNs as Fig. S15 where ACaPPi is in inner space and is coated by ACaPi on the surface.

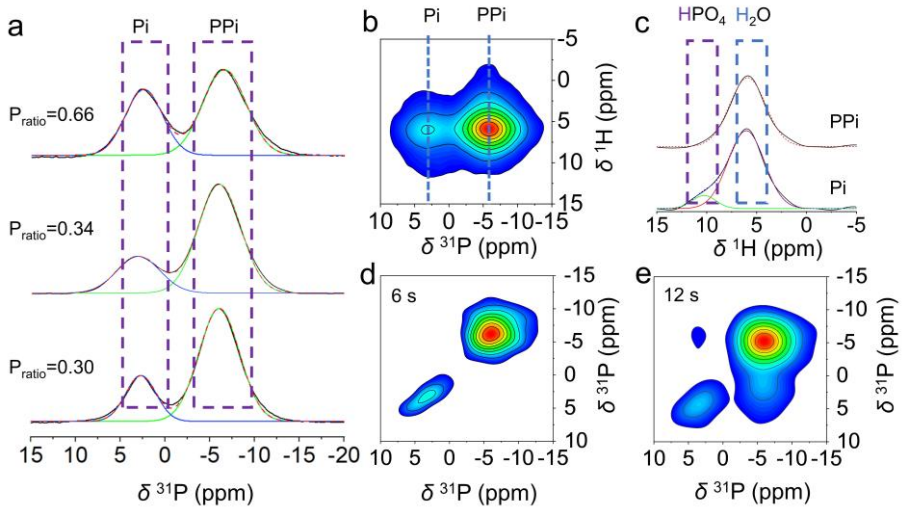

Fig. 4. Solid state nuclear magnetic resonance analysis of ACPPNs. (a) ^{31}P MAS NMR spectra. The measured nanowires are prepared at Ca/P=0.1 (top, same as the sample in Fig.1), at Ca/P=0.1 with PMA (middle, same as the sample in Fig.2a), and at Ca/P=0.025 (bottom, same as the sample in Fig.3b), respectively. Black solid curve: original spectrum; blue and green curve: Gaussians from the deconvolution of the original spectrum; red dashed curve: the sum of the Gaussians. The P_{ratio}, ratio of P_e in Pi and PPi, is shown for the corresponding spectrum of each sample. Dashed rectangles indicate the chemical shifts attributed to Pi and PPi as indicated. (b) 2D ^{1}H-^{31}P HETCOR CPMAS NMR spectra of ACPPNs prepared at Ca/P=0.025. (c) Extracted cross-section ^{1}H spectra at the ^{31}P chemical shifts of Pi and PPi as indicated in the dashed line of (b). Dashed rectangles show the resonance of H from H_2O and HPO_4^{2-}, respectively. (d, e) ^{31}P-^{31}P NOESY CPMAS NMR spectra (same sample as b) at mixing times of 6s (d) and 12s (e).

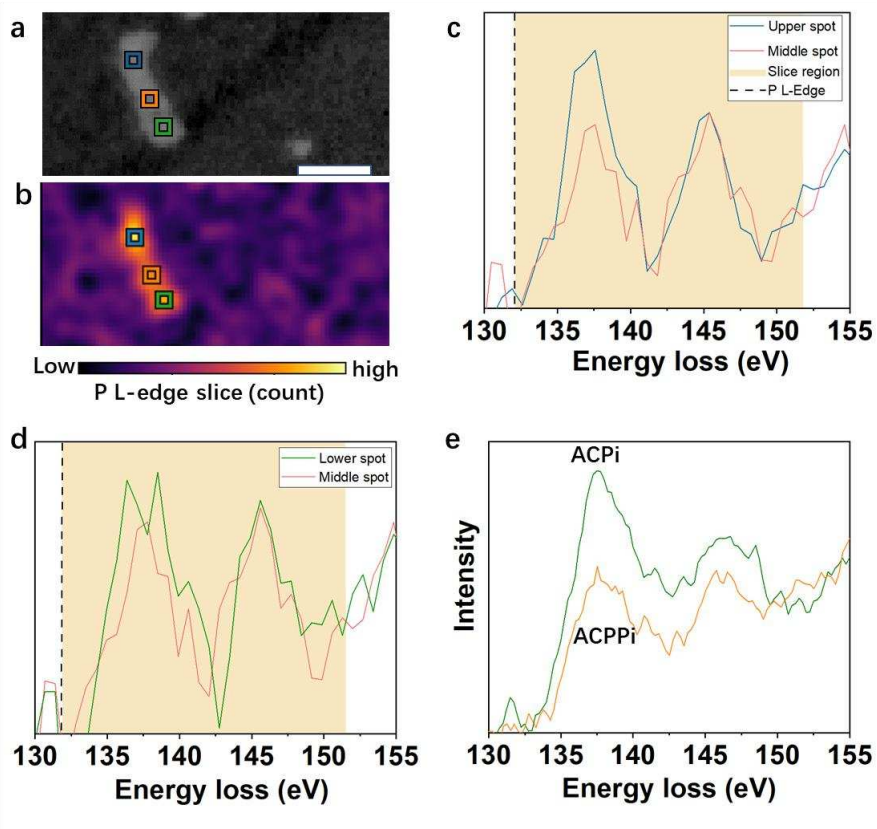

Fig. 5. STEM-EELS analysis on ACPPNs. (a) HAADF image (upper) of a short-rod-like structure used to acquire P EELS. Due to the low signal intensity of thin nanowires, a thicker rod was selected for measurements (thus, the structural differences between thick and thin nanowires can not be ruled out). Scale bar: 50 nm. (b) Background-subtracted, smoothed, spectrum image (SI) slice of the P L-Edge on the ACPPN rod. (c, d) Representative EEL spectra from the regions marked in (a) and (b). The relative intensities of the peaks at 138 eV and 146 eV, corresponding to the L_2 and L_3 peaks, vary between the spots. The significant changes of the L_2:L_3 ratio, e.g., upper spot VS middle spot (c) and lower spot VS middle spot (d), indicate fundamental changes in the P bonding of the inner and outer spaces of ACPPNs. (e) EELS of ACPi and ACPPi. The difference of the L_2:L_3 ratio between the two specimens is consistent with that of (b) and (c), which thus corroborates the anisotropic distribution of Pi and PPi. We convolved the spectrum image with a gaussian of about 15 pixel diameter to retain the spatial information but obtain a better signal-to-noise ratio.

2.3 Formation mechanism of ACPPNs—oriented growth

The formation process of ACPPNs

We investigated the formation process of ACPPNs by tracking the evolution of the formed species in the reaction solutions. As the process takes about 5 minutes in the presence of PMA (Ca/P=0.1) to form visible precipitation after adding the P_e source due to its inhibitory effect on the nucleation, which is a much slower reaction than that without polymers (immediate precipitation), it becomes possible to characterize intermediate species of the reaction. Therefore, we first studied the formation process involving inhibitor PMA by cryo-TEM. It shows that, 5 min after P_e addition, nanoclusters with a size of ~1-2 nm are obtained, and some of them begin to aggregate or assemble into short nanorods (Fig. 6a); 10 min after P_e addition (Fig. 6b), nanowires with a diameter of ~2 nm, which is similar to that of the former nanoclusters, are predominant in the micrographs. Moreover, in some nanowires, which should be the early formed ones, distinct boundaries in between the nanoclusters are observed. The FTIR spectra show that the ratio of Pi and PPi does not change very much during the ACPPNs formation according to the relative intensities of corresponding bands, which also reveals that Pi and PPi simultaneously react with Ca^{2+} in the solution instead one by one. (Fig. S16a). Therefore, for the formation process, nanoclusters with a size of 1-2 nm are formed in the solution first, after adding P_e; then, they aggregate into short rods; finally, the rods grow into nanowires by attaching more nanoclusters (Fig. 7).

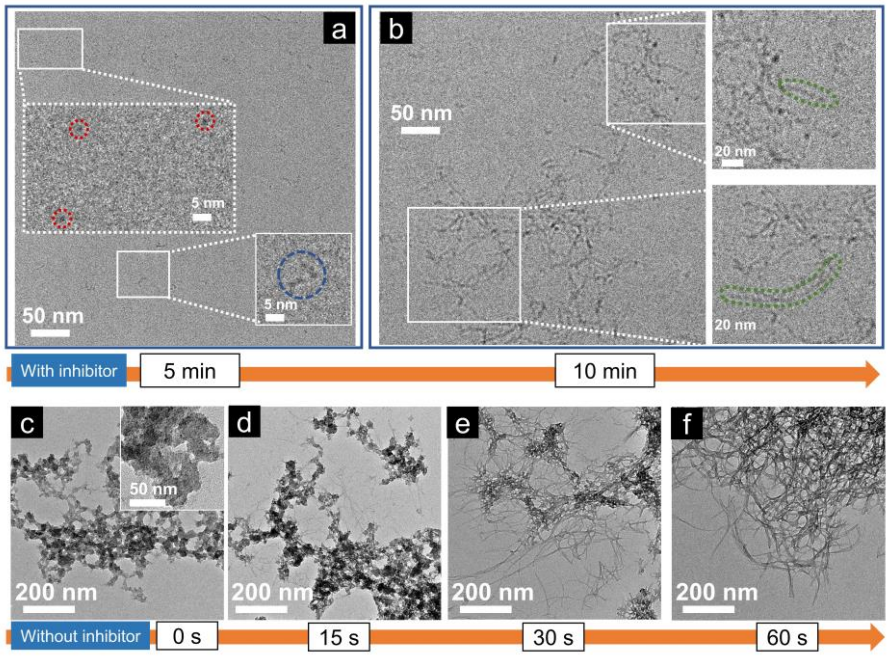

Fig. 6. Study of the ACPPNs formation mechanism. (a, b) Cryo-TEM images of the formed species in the solution at 5 min (a) and 10 min (b) during the PMA (Ca/P=0.1) involved process. The magnified area indicated by dashed circles highlight single nanocluster [64], short nanorods (blue), and long nanowires (green) formed by oriented aggregation in 1-D. (c-f) TEM images of the formed species in the solution at different times during the process of Ca/P=0.025 as indicated.

The formation of ACPPNs without polymer inhibitors progresses so rapidly that precipitation occurs as soon as P_e is added. Thus, the question whether nanowires are formed immediately or after a certain lag time spurs us to investigate the formation progress at Ca/P=0.025. Fig. 6c shows that only nanoparticles, which seem to be built up by nanocluster aggregation, are observed in the sample at 0 s. Over time, nanowires appear at 15 s, with their fraction increasing afterwards, and dominating at 60 s (Fig. 6d-f). This indicates that the nanowires are formed at the expense of nanoparticles. Again, FTIR spectra of the samples at different time points do not vary significantly over time indicating that the chemical compositions remain largely unchanged (Fig. S16b). Therefore, in this system, nanoclusters are formed first, but instead of subsequent aggregating in 1-D (like in the presence of PMA), they then quickly

aggregate into nanoparticles. However, the nanoparticles finally transform into nanowires by rearrangement or a dissolution-reprecipitation process (Fig. 7). It is reasonable to understand the aggregation of early formed nanoclusters: without nucleation inhibitor and stabilizer like PMA, a large number of nanoclusters are formed in a very short time, which tend to first randomly aggregate due to the high specific surface area and high surface free energy.

Besides, when tracking the transformation process with P_e addition in the sequence of PPi-and-Pi by Cryo-TEM, we find that nanowires are formed via the transformation of nanoparticles as well after adding Pi (Fig. S17).

The transformation of nanoparticles into nanowires at later stages indicates that nanowire formation should be controlled by thermodynamics rather than kinetics, that is, the nanowires seem to be more thermodynamically favored than nanoparticles in the long term, although we cannot categorically rule out that also kinetic aspects play a role.

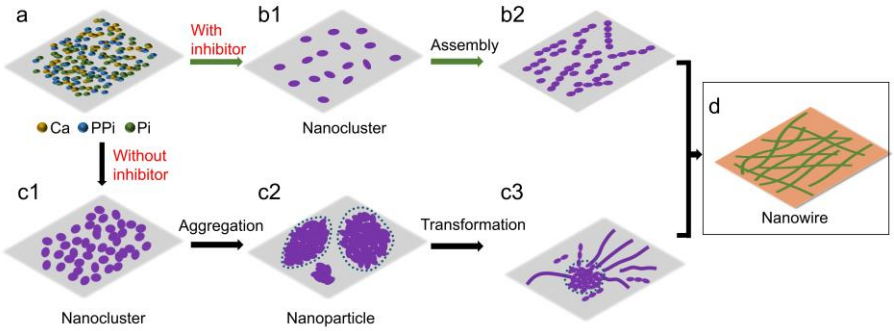

Fig. 7. Schematic illustration of possible ACPPNs formation pathways with nucleation inhibitor (PMA) and without nucleation inhibitor. In the presence of nucleation inhibitor, ions (a) react to form nanoclusters with a size of 1-2 nm (b1) firstly after adding the P_e source; then, they aggregate into short rods (b2); and finally grow into nanowires (d). However, for ACPPNs preparation without nucleation inhibitor, nanoclusters are formed first (c1), then quickly aggregate into nanoparticles (c2), but finally transform into nanowires (c3) by rearrangement or a dissolution-reprecipitation process.

The cause for the oriented growth of ACPPNs

It has been established that, in crystals, the energy differences between different

facets, drives the preferential growth according to Wulff's rule [65], leading to certain facets exposed on the surface of crystals, forming distinct planes, angles, and edges. However, it is surprising that ACPPNs, with an amorphous phase confirmed by multiple characterizations, grow into this 1-dimensional structure instead of nanospheres or irregular aggregates of nanoparticles without any external regulation. We also exclude the effect of mechanical shear stress of stirring, by obtaining nanowires without stirring after P_e addition (Fig. S18). Generally, the amorphous solids exhibit the order in their microstructure only within a very short range [52], where the atoms and ions are, on average of nanometer scale and shorter, uniformly distributed in the solids [37, 51]. So, when the amorphous solids grow by either attaching nanosized particles or atoms/ions, there are no energy differences between each spatial direction, that is, all directions are equally favored by the atoms and ions during attachment. This should, like in the other amorphous solids, lead to the morphologies of nanospheres or irregular aggregates of nanoparticles. Thus, the fact that we obtain nanowires with such high aspect ratio expands this conventional view.

Considering that various preparation conditions (high or low Ca/P ratio, one-step, two-step, with or without polymers, P_e addition of PPi-and-Pi), and different intermediate states (nanoclusters and nanoparticles with different compositions) all result in ACPPNs formation, the growth of the nanowire should be mainly driven by its inherent properties. Therefore, it is reasonable to propose that the anisotropy of the ACPPNs microstructure causes the oriented growth. As discussed above, the anisotropic distribution of Pi and PPi within the nanowires has been corroborated by ^{31}P MAS NMR spectra (Fig. 4) and STEM-EELS (Fig. 5, Fig S14), and is consistent with the fact that the specific addition sequence of PPi-and-Pi is important for yielding nearly exclusively nanowires (Fig. S12). Thus, during the growth, the building units (ions or nanoclusters) attach to the nanowire in a preferential rather than random way, depending on the energy differences as shown in Fig. S19. A similar mechanism is also seen in an organic system (but not in amorphous inorganic ones): the core-shell

structured cylindrical micelles, where the inner core and outer shell consist of distinct components and drive the 1-D oriented growth[66].

As for the possible anisotropy in the nanoclusters, we can hardly determine it by experimental characterizations due to their transient state in the solution and very small size. Actually, it is believed that some amorphous solids are composed of clusters with specific structures whose sizes are comparable to the short order range, for example, the so-called Posner's cluster or CHPC cluster [67]. Also, anisotropy of a special ACaPi building block stabilized by a small molecule was indicated by Tang et al. [68-69]. In their work, linear ion oligomers of amorphous calcium phosphate were prepared, where the chemical environment of ends and middle segments are obviously different. However, oligomer attachment did not occur in 1-dimension during the growth, and nanowires were not observed. As for ACaPPi, its microstructure has been much less studied than that of ACaPi. Although an order range of 8 Å was indicated by the pair distribution function pattern[17], potential anisotropy was not studied further. These all indicate that, within the size of short and medium range order, anisotropic nanoclusters could be formed. In the nanoclusters-involved ACPPNs growth, beside the anisotropic nanowires, Ca, Pi, PPi, and H_2O should also have formed anisotropic building blocks, *i.e.*, the nanoclusters, with a heterogeneous distribution of components. In this sense, our observations may again resemble the formation of core-shell structured cylindrical micelles[66]. That is, the nanoclusters can be regarded as inorganic analogues of amphiphilic organic diblock copolymers, or surfactants, which subsequently self-assemble. Please note that the formation of ACPPNs is not dependent on the presence of organic amphiphiles, but an analogous, purely amorphous inorganic phenomenon.

Moreover, the rather slow assembly velocity of building blocks seems necessary for the nanowire formation. Otherwise, the building blocks do not have sufficient time for direction selection to form nanowires. In the case of PMA and PAA involved reaction, it takes more than 5 minutes to initiate nucleation and further 10 minutes to finish the assembly; in the case without polymers, 1 min is needed to transform

nanoparticles into nanowires. This also inspires us that, a slow transformation from one amorphous solid to another amorphous one, may proceed via oriented growth as well in other materials.

3. Conclusion

The amorphous calcium phosphate-pyrophosphate nanowires (ACPPNs) are formed via an oriented growth in the aqueous regulator-free solution containing Ca^{2+}, Pi, and PPi. It is composed of amorphous calcium phosphate and amorphous calcium pyrophosphate and displays the morphology of highly elongated nanowires with an average diameter of ~2-3 nm, and lengths of up to hundreds of nanometers. Their amorphous phase are confirmed in multiple ways. Both Pi and PPi are indispensable for the formation of nanowires, in which the ACaPi and ACaPPi are distributed at separated sites but stay close to each other. Further studies show that the ACPPNs form via either the preferential attachment of ~2 nm nanoclusters in a 1-dimension fashion (in the presence of nucleation inhibitor), or the transformation of bigger nanoparticles (without nucleation inhibitor). An anisotropy of the ACPPNs microstructure should cause their preferential growth, which is rarely seen in inorganic amorphous solids. This proves that, unlike the conventional view, amorphous solids can form via oriented growth, expanding the conventional view on the structure and growth behavior of amorphous minerals. This finding may also provide a new perspective for biomineral growth in vivo, which will be studied in the future. On the other hand, given the flectional morphology in the TEM images and the possible micelle-like growth behavior of ACPPNs, they display the characters of organic polymers. This work, along with previous reports such as amorphous inorganic oligomers[69] and sub-one-nanometer inorganic materials[70], inspires us to further explore the organics-like behaviors in inorganic substances.

Due to technical limitations, characterizing the microstructure of amorphous solids remains a great challenge. Therefore, the specific arrangements of the ions in ACPPNs

were not determined in this study. We also would like to remind that, during this study, we found significant content of impurity PPi in the chemical Na_2HPO_4 (analytical grade) from different commercial suppliers, which may have impacted or will further affect the results of researches.

4. Experimental Procedures

4.1 Materials

Sodium pyrophosphate ($Na_4P_2O_7$, PPi source) was purchased from Aladdin Biochemical Technology Co., China. Sodium phosphate dibasic (Na_2HPO_4, Pi source) was purchased from Sigma-Aldrich. Calcium chloride dihydrate ($CaCl_2 \cdot 2H_2O$)was purchased from Sinopharm Chemical Reagent Co., China. Glycerin, sodium polyacrylate (PAA, 50% in H_2O, Mw 3000-5000), and polymaleic acid (PMA, 50% in H_2O, Mw 400-800) were purchased from Macklin Biochemical Co., China. All the chemicals were used without further processing.

4.2 Preparation of calcium phosphate-pyrophosphate nanowires (ACPPNs)

ACPPNs are prepared by simply mixing the solutions of calcium source (Ca^{2+}) and phosphorus source (Pi and PPi, denoted as P_e), where the amount of Ca^{2+} is fixed at 1.00 mmol, but that of Pe is varied.

Preparation of ACPPNs at high atomic ratio of Ca/P (>0.05) by a two-step procedure

Typically, three solutions were prepared as follows: 1.00 mmol of $CaCl_2 \cdot 2H_2O$ was dissolved in 100 ml of deionized water (solution A, 0.01 M); 5.00 mmol P_e source with 15% in the form of PPi (0.375 mmol $Na_4P_2O_7$) and 85% in the form of Pi (4.25 mmol Na_2HPO_4) was dissolved in 50 ml of deionized water (solution B, 0.1M), and another 5.00 mmol P_e source with same Pi/PPi ratio in 5 ml deionized water (solution C, 1M), respectively. All the pH of the solutions was adjusted to 8.00 using 1M HCl and NaOH solutions. Under vigorous stirring, mix solutions A and B and adjust the pH to 8.00, then add solution C and keep the pH at 8.00 during the reaction. The two-step procedure can facilitate the control over the pH of the reaction solution. After the

reaction, the solution was centrifuged at 7000 rpm for 1 min, and the precipitation was washed with deionized water for 5 times and absolute ethanol for twice. All procedures were conducted at ambient temperature.

The ratio of P_e forms (Pi and PPi) was varied (P_e of PPi: 0, 5, 10, 15, 25, 100%) while other conditions kept the same as above to investigate the effects on the morphology of ACPPNs. For 100% PPi (only PPi as the P_e), as the solubility of PPi source, sodium pyrophosphate, in H_2O is too low to prepare solution C (https://cameochemicals.noaa.gov/chemical/25074), so the saturated PPi solution was used.

For the PAA involved preparation, 0.40 ml PAA (50% in H_2O, Mw 3000-5000) was added into solution A, and other conditions were the same as above. For the PMA (50% in H_2O, Mw 400-800) involved in the preparation, 1.20 ml PMA was added into solution A, and the solvent in solution A was replaced by a mixed one of 80 mL water + 20 mL glycerol. Other conditions were the same as above.

Preparation of ACPPNs at low atomic ratio of Ca/P (≤0.05) by a one-step procedure

Based on the procedure above, all of the P_e was dissolved only in solution B, and the addition of P_e was finished in one step (instead of two). Other conditions remained the same as above.

As the amount of P_e is much higher than Ca, the effect of chemical reaction on the pH is negligible, and it is not very necessary to adjust pH during the reaction. Therefore, one-step method was used when adding high (≥20 mmol) amount of P_e (Ca/P ≤ 0.05).

To investigate the formation progress, at a specific time point, 0.5 mL reaction solution was quenched with 5.0 mL ethylene glycol, then immediately centrifuged at 12000 rpm for 1 min, washed with ethylene glycol for 3 times, and absolute ethanol for 3 times. The samples were characterized for TEM or FTIR (after drying in vacuum).

As the controls for characterizations, ACPi with the P_e in the form of HPO_4^-(same as this work) was prepared following the previous protocol[38]: Na_2HPO_4 (0.95 mmol)

and $Na_3PO_4 \cdot 12H_2O$ (0.05 mmol) was dissolved in 3 mL deionized water, then quickly added into 2 mL $CaCl_2$ (1.67 mmol) aqueous solution. After 3 s, 80 mL methanol was added to quench the reaction; ACPPi was prepared via the protocol same as that of Fig. 4F.

ACPPNs formation when adding Pi and PPi in separate steps

The protocol follows that of a two-step procedure with modifications. Three solutions were prepared as follows: 1.00 mmol of $CaCl_2 \cdot 2H_2O$ was dissolved in 100 ml of deionized water (Ca solution, 0.01M); 0.75 mmol PPi was dissolved in 10 ml deionized water (PPi solution, 0.075M); 8.50 mmol Pi was dissolved in 50 ml deionized water (Pi solution, 0.17M). In the Ca solution, Pi and PPi in separate steps: add PPi and Pi solution successively (PPi-and-Pi) with 3 s interval; add Pi and PPi solution successively (Pi-and-PPi) with 3 s interval; add PPi solution, separate the precipitation by centrifugation, wash it with H_2O, then add Pi solution (PPi-and-Pi); add Pi solution, separate the precipitation by centrifuge, wash it with H_2O, then add PPi solution. All of the resulting precipitates were separated by centrifugation and washed with deionized water and absolute ethanol.

4.3 Solid state nuclear magnetic resonance spectroscopy

Solid state nuclear magnetic resonance characterization, including 1D ^{31}P and ^{1}H magic angle spinning (MAS), 2D ^{1}H-^{31}P Heteronuclear Correlation (HETCOR) CPMAS NMR, 2D ^{31}P–^{31}P Nuclear Overhauser exchange (NOESY) CPMAS NMR were conducted using a Bruker AVANCE-III 400MHz widebore spectrometer. The frequency of magic angle spinning was 25 kHz. $NH_4H_2PO_4$ and adamantane were used as references for ^{31}P and ^{1}H MAS NMR, respectively. Fine powdered samples were filled in the rotor with a diameter of 1.9 mm, and then directly measured. The NMR peaks were integrated after deconvolution for quantitative calculations.

4.4 Transmission electron microscopy (TEM)

The samples were dispersed in absolute ethanol, then dropped on a carbon coated copper grids, and finally measured with the Transmission electron microscope (JEM-2100F and FEI Tecnai G2 F20).

4.5 Cryogenic -transmission electron microscopy (Cryo-TEM)

2 μL aqueous samples solution were taken for cryo-electron microscopy. After dropping on a plasma treated grid, it was quickly vitrified using automated vitrification robot (Vitrobot Mark IV/Leica EM GP2) with blot time of 5 s, wait time of 1 s, and drain time of 0s. The sample was characterized using Thermo-Fisher Transmission Electron Microscope (Talos L120C G2) for observation.

4.6 Electron Energy-Loss Spectroscopy (EELS)

The data EELS was acquired on a Nion High Energy Resolution Monochromated STEM-EELS operating at 60 kV equipped with a Dectris ELA direct electron detector. Samples were cooled to a temperature of 100 °K using a Gatan Elsa single tilt holder to mitigate beam damage. Light monochromation was used to reduce the fill-width at half-maximum of the electron beam to ~ 100 meV, which resulted in a beam current of ~30 pA. A convergence semiangle of 30 mrad and a collection semiangle of 25 mrad was used for the experiment. Spectra were background fitted with a powerlaw from two background fit regions (125-130 eV before P L-Edge, and 270-280 eV before C K-Edge). Spectra were also filtered with a Gaussian-averaging-kernel with a sigma of 15 pixels to improve signal to noise.

4.7 X-ray powder diffraction (XRD)

The XRD patterns were acquired by Rigaku Ultimate IV powder X-ray Cu Ka radiation diffractometer (λ=1.5418A) with voltage of 40 kV, current of 40 mA, scanning angle of 2θ = 5–80°, and scanning speed of 10°/min.

4.8 Fourier transform infrared spectroscopy (FTIR)

FTIR was obtained using a spectrometer (Nicolet IS50, Thermo Scientific; IRSpirit, SHIMADZU) by following the KBr technique. KBr and the sample mixture at a ratio of 100:2 were pressed into plates for measurement.

4.9 Thermogravimetric analysis (TGA)

TGA measurements were performed by the analyzer (NETZSCH STA 409 PC/PG) in the air atmosphere and the heating rate was 10 ^{o}C/min. 10-20 mg of powder samples were used for testing.

4.10 X-Ray Photoelectron Spectroscopy (XPS)

XPS was collected by a spectrometer (Thermo Scientific K-Alpha) with Al Kα X-rays (hν = 1486.6 eV) at 12 kV and 6 mA. All high-resolution spectra were recorded at a pass energy of 1 eV. Sample charging was corrected by setting the lowest BE component of the C1s spectral envelope to 284.80 eV.

4.11 Inductively Coupled Plasma Optical Emission Spectrometry (ICP-OES)

The powder samples were dissolved in 1% HNO_3 to determine their elemental composition using an Inductively Coupled Plasma Optical Emission Spectrometry (Agilent 5100).

4.12 Small-angle X-ray scattering (SAXS) and wide-angle X-ray scattering (WAXS)

The SAXS/WAXS experiments were conducted at the JCNS MLZ using a laboratory-based SAXS-WAXS beamline, KWS-X (XENOCS XUESS 3.0 XL). The sample prepared Ca/P =0.025 (P_e=40 mmol) via a one-step procedure, and dispersed ethanol for measurements. A MetalJet X-ray source (Excillum D2+) with a liquid metal anode operated at 70 kV and 3.57 mA, emitting Ga-Kα radiation with a wavelength (λ) of 1.314 Å. Solution samples were measured in a sealed glass capillary (2 mm diameter and 0.05mm thickness) at the capillary. The sample-to-detector distances ranged from 0.1 m to 1.70 m, covering the scattering vector Q range from 0.003 to 4.5 Å-1 (Q is the scattering vector, $Q=(4\pi/\lambda)\sin(\theta)$, where 2θ represents the scattering angle). The SAXS patterns were normalized to an absolute scale, and azimuthally averaged to obtain the intensity profiles. Ethanol as background was subtracted.

Acknowledgements

This work was supported by the National Natural Science Foundation of China (Nos. 31771081), the Science and Technology Commission of Shanghai Municipality (Nos. 21ZR1449700 and 19441901900), and the SuperSTEM is the UK national facility for Advanced Electron Microscopy Funded by EPSRC (EP/W021080/1).

We thank Dr. Ruijuan Qi, Dr. Yanping Sui, and Dr. Chunlei Zhang for helping with TEM characterizations. EELS measurements were conducted at the Center for Nanophase Materials Sciences (CNMS), which is a DOE Office of Science User Facility using instrumentation within ORNL's Materials Characterization Core provided by UT-Battelle, LLC, under Contract No. DE-AC05-00OR22725 with the DOE and sponsored by the Laboratory Directed Research and Development Program of Oak Ridge National Laboratory, managed by UT-Battelle, LLC, for the U.S. Department of Energy. Solid state NMR was conducted by Dr. Ming Shen and supported by the Open Project of Shanghai Key Laboratory of Magnetic Resonance in East China Normal University (SKMR2023A02). We also thank the China Scholarship Council for the support during Chaobo Feng's visit to Leibniz University Hannover (202206260260).

References

1. Florencio-Silva, R.; Sasso, G. R.; Sasso-Cerri, E.; Simões, M. J.; Cerri, P. S., Biology of Bone Tissue: Structure, Function, and Factors That Influence Bone Cells. *Biomed. Res. Int.* **2015,** *2015*, 421746.
2. Wang, X. M.; Zhao, D. C.; Ren, H. H.; Yan, Y. G.; Li, S. Y., Biological evaluation of the modified nano-amorphous phosphate calcium doped with citrate/poly-amino acid composite as a potential candidate for bone repair and reconstruction. *J. Mater. Sci.-Mater. Med.* **2021,** *32* (1), 18.
3. Meyer, F.; Amaechi, B. T.; Fabritius, H. O.; Enax, J., Overview of Calcium Phosphates used in Biomimetic Oral Care. *Open Dent. J* **2018,** *12*, 406-423.
4. Abou Neel, E. A.; Aljabo, A.; Strange, A.; Ibrahim, S.; Coathup, M.; Young, A. M.; Bozec, L.; Mudera, V., Demineralization-remineralization dynamics in teeth and bone. *Int. J. Nanomed.* **2016,** *11*, 4743-4763.
5. Wang, L.; Nancollas, G. H., Calcium Orthophosphates: Crystallization and Dissolution. *Chem. Rev* **2008,** *108* (11), 4628-4669.
6. Villa-Bellosta, R.; O'Neill, W. C., Pyrophosphate deficiency in vascular

calcification. *Kidney Int.* **2018,** *93* (6), 1293-1297.
7. Gohr, C., In vitro models of calcium crystal formation. *Curr. Opin. Rheumatol.* **2004,** *16* (3), 263-267.
8. Rosenthal, A. K., Update in calcium deposition diseases. *Curr. Opin. Rheumatol.* **2007,** *19* (2), 158-162.
9. Iqbal, S. M.; Qadir, S.; Aslam, H. M.; Qadir, M. A., Updated Treatment for Calcium Pyrophosphate Deposition Disease: An Insight. *Cureus* **2019,** *11* (1), e3840.
10. McCarthy, G. M.; Dunne, A., Calcium crystal deposition diseases — beyond gout. *Nat. Rev. Rheumatol* **2018,** *14* (10), 592-602.
11. Nguyen, C.; Bazin, D.; Daudon, M.; Chatron-Colliet, A.; Hannouche, D.; Bianchi, A.; Côme, D.; So, A.; Busso, N.; Busso, N.; Lioté, F.; Ea, H. K., Revisiting spatial distribution and biochemical composition of calcium-containing crystals in human osteoarthritic articular cartilage. *Arthritis Res. Ther.* **2013,** *15* (5), R103.
12. Giachelli, C. M.; Speer, M. Y.; Li, X. W.; Rajachar, R. M.; Yang, H., Regulation of vascular calcification - Roles of phosphate and osteopontin. *Circ. Res* **2005,** *96* (7), 717-722.
13. Voelkl, J.; Lang, F.; Eckardt, K.-U.; Amann, K.; Kuro-o, M.; Pasch, A.; Pieske, B.; Alesutan, I., Signaling pathways involved in vascular smooth muscle cell calcification during hyperphosphatemia. *Cell Mol. Life Sci* **2019,** *76* (11), 2077-2091.
14. Jaovisidha, K.; Rosenthal, A. K., Calcium crystals in osteoarthritis. *Curr. Opin. Rheumatol.* **2002,** *14* (3), 298-302.
15. Terkeltaub, R. A., Inorganic pyrophosphate generation and disposition in pathophysiology. *Am. J. Physiol. Cell Physiol.* **2001,** *281* (1), C1-C11.
16. Johnson, K.; Jung, A.; Murphy, A.; Andreyev, A.; Dykens, J.; Terkeltaub, R., Mitochondrial oxidative phosphorylation is a downstream regulator of nitric oxide effects on chondrocyte matrix synthesis and mineralization. *Arthritis. Rheum.* **2000,** *43* (7), 1560-1570.
17. Slater, C.; Laurencin, D.; Burnell, V.; Smith, M. E.; Grover, L. M.; Hriljac, J. A.; Wright, A. J., Enhanced stability and local structure in biologically relevant amorphous materials containing pyrophosphate. *J. Mater. Chem* **2011,** *21* (46), 18783-18791.
18. Nagasaki, A.; Nagasaki, K.; Chu, E. Y.; Kear, B. D.; Tadesse, W. D.; Ferebee, S. E.; Li, L.; Foster, B. L.; Somerman, M. J., Ablation of Pyrophosphate Regulators Promotes Periodontal Regeneration. *J. Dent. Res.* **2021,** *100* (6), 639-647.
19. Anderson, H. C.; Garimella, R.; Tague, S. E., The role of matrix vesicles in growth plate development and biomineralization. *Front Biosci.* **2005,** *10*, 822-37.
20. Orriss, I. R.; Arnett, T. R.; Russell, R. G., Pyrophosphate: a key inhibitor of mineralisation. *Curr. Opin. Pharmacol.* **2016,** *28*, 57-68.
21. Fleisch, H.; Russell, R. G.; Straumann, F., Effect of pyrophosphate on hydroxyapatite and its implications in calcium homeostasis. *Nature* **1966,** *212* (5065), 901-3.
22. Fleisch, H.; Bisaz, S., Isolation from urine of pyrophosphate, a calcification

inhibitor. *Am. J. Physiol.* **1962,** *203*, 671-5.
23. Fleisch, H.; Straumann, F.; Schenk, R.; Bisaz, S.; Allgöwer, M., Effect of condensed phosphates on calcification of chick embryo femurs in tissue culture. *Am. J. Physiol.* **1966,** *211* (3), 821-5.
24. Ibsen, C. J. S.; Birkedal, H., Pyrophosphate-Inhibition of Apatite Formation Studied by In Situ X-Ray Diffraction. *Minerals* **2018,** *8* (2), 65.
25. Fleisch, H.; Bisaz, S., Mechanism of Calcification: Inhibitory Role of Pyrophosphate. *Nature* **1962,** *195* (4844), 911-911.
26. Zhou, X.; Cui, Y.; Zhou, X.; Han, J., Phosphate/Pyrophosphate and MV-related Proteins in Mineralisation: Discoveries from Mouse Models. *Int. J. Biol. Sci.* **2012,** *8* (6), 778-790.
27. Murshed, M.; Harmey, D.; Millán, J. L.; McKee, M. D.; Karsenty, G., Unique coexpression in osteoblasts of broadly expressed genes accounts for the spatial restriction of ECM mineralization to bone. *Genes Dev.* **2005,** *19* (9), 1093-104.
28. Thouverey, C.; Bechkoff, G.; Pikula, S.; Buchet, R., Inorganic pyrophosphate as a regulator of hydroxyapatite or calcium pyrophosphate dihydrate mineral deposition by matrix vesicles. *Osteoarthritis Cartilage* **2009,** *17* (1), 64-72.
29. Millán, J. L., The Role of Phosphatases in the Initiation of Skeletal Mineralization. *Calcif. Tissue Int* **2013,** *93* (4), 299-306.
30. De Yoreo, J. J.; Gilbert, P. U. P. A.; Sommerdijk, N. A. J. M.; Penn, R. L.; Whitelam, S.; Joester, D.; Zhang, H.; Rimer, J. D.; Navrotsky, A.; Banfield, J. F.; Wallace, A. F.; Michel, F. M.; Meldrum, F. C.; Cölfen, H.; Dove, P. M., Crystallization by particle attachment in synthetic, biogenic, and geologic environments. **2015,** *349* (6247), aaa6760.
31. Wang, Y.; Dai, L.; Ding, Z.; Ji, M.; Liu, J.; Xing, H.; Liu, X.; Ke, Y.; Fan, C.; Wang, P.; Tian, Y., DNA origami single crystals with Wulff shapes. *Nat. Commun.* **2021,** *12* (1), 3011.
32. Wulff, G., XXV. Zur Frage der Geschwindigkeit des Wachsthums und der Auflösung der Krystallflächen. *Cryst. Mater.* **1901,** *34* (1-6), 449-530.
33. Li, R.; Zhang, X.; Dong, H.; Li, Q.; Shuai, Z.; Hu, W., Gibbs–Curie–Wulff Theorem in Organic Materials: A Case Study on the Relationship between Surface Energy and Crystal Growth. **2016,** *28* (8), 1697-1702.
34. Jehannin, M.; Rao, A.; Cölfen, H., New Horizons of Nonclassical Crystallization. *J. Am. Chem. Soc.* **2019,** *141* (26), 10120-10136.
35. Gebauer, D.; Wolf, S. E., Designing Solid Materials from Their Solute State: A Shift in Paradigms toward a Holistic Approach in Functional Materials Chemistry. *J. Am. Chem. Soc.* **2019,** *141* (11), 4490-4504.
36. Weiner, S.; Addadi, L., Crystallization Pathways in Biomineralization. *Annu. Rev. Mater. Res.* **2011,** *41* (1), 21-40.
37. Dorozhkin, S. V., Amorphous calcium (ortho)phosphates. *Acta Biomater.* **2010,** *6* (12), 4457-4475.
38. Lu, B.-Q.; Willhammar, T.; Sun, B.-B.; Hedin, N.; Gale, J. D.; Gebauer, D.,

Introducing the crystalline phase of dicalcium phosphate monohydrate. *Nat. Commun* **2020,** *11* (1), 1546.
39. Meldrum, F. C.; Cölfen, H., Controlling mineral morphologies and structures in biological and synthetic systems. *Chemical reviews* **2008,** *108* (11), 4332-432.
40. Gelli, R.; Ridi, F.; Baglioni, P., The importance of being amorphous: calcium and magnesium phosphates in the human body. *Adv. Colloid Interface Sci* **2019,** *269*, 219-235.
41. Gelli, R.; Briccolani-Bandini, L.; Pagliai, M.; Cardini, G.; Ridi, F.; Baglioni, P., Exploring the effect of Mg2+ substitution on amorphous calcium phosphate nanoparticles. *J. Colloid Interface Sci* **2022,** *606*, 444-453.
42. Combes, C.; Rey, C., Amorphous calcium phosphates: Synthesis, properties and uses in biomaterials. *Acta Biomater.* **2010,** *6* (9), 3362-3378.
43. Jin, B.; Liu, Z.; Shao, C.; Chen, J.; Liu, L.; Tang, R.; De Yoreo, J. J., Phase Transformation Mechanism of Amorphous Calcium Phosphate to Hydroxyapatite Investigated by Liquid-Cell Transmission Electron Microscopy. *Cryst. Growth & Des* **2021,** *21* (9), 5126-5134.
44. Borovik, P.; Oestreicher, V.; Huck-Iriart, C.; Jobbágy, M., Amorphous Calcium Phosphates: Solvent-Controlled Growth and Stabilization through the Epoxide Route. *Chem. Eur. J* **2021,** *27* (39), 10077-10086.
45. Gower, L. B., Biomimetic model systems for investigating the amorphous precursor pathway and its role in biomineralization. *Chem. Rev* **2008,** *108* (11), 4551-627.
46. Tao, J.; Pan, H.; Zeng, Y.; Xu, X.; Tang, R., Roles of Amorphous Calcium Phosphate and Biological Additives in the Assembly of Hydroxyapatite Nanoparticles. *J. Phys. Chem. B* **2007,** *111* (47), 13410-13418.
47. Yi, D.; Xu, C.; Tang, R.; Zhang, X.; Caruso, F.; Wang, Y., Synthesis of Discrete Alkyl-Silica Hybrid Nanowires and Their Assembly into Nanostructured Superhydrophobic Membranes. **2016,** *55* (29), 8375-8380.
48. Zhou, W.; Liu, Q.; Huang, Q., Reversing silicon carbide into 1D silicon nanowires and graphene-like structures using a dynamic magnetic flux template. *Materials Horizons* **2023,** *10* (4), 1354-1362.
49. Adachi, M. M.; Anantram, M. P.; Karim, K. S., Optical Properties of Crystalline−Amorphous Core−Shell Silicon Nanowires. *Nano Lett.* **2010,** *10* (10), 4093-4098.
50. Huang, J. Y.; Chen, S.; Ren, Z. F.; Chen, G.; Dresselhaus, M. S., Real-Time Observation of Tubule Formation from Amorphous Carbon Nanowires under High-Bias Joule Heating. *Nano Lett.* **2006,** *6* (8), 1699-1705.
51. Meldrum, F. C.; Cölfen, H., Controlling mineral morphologies and structures in biological and synthetic systems. *Chem. Rev.* **2008,** *108* (11), 4332-432.
52. Dorozhkin, S. V., Calcium orthophosphates (CaPO4): occurrence and properties. *Prog. Biomater.* **2016,** *5* (1), 9-70.
53. Gülseren, O.; Ercolessi, F.; Tosatti, E. J. P. R. L., Noncrystalline structures of

ultrathin unsupported nanowires. **1998,** *80* (17), 3775.
54. Zhang, S.; Wang, X. J. A. M. L., Sub-one-nanometer nanomaterials showing polymer-analogue properties. **2020,** *2* (6), 639-643.
55. Cademartiri, L.; Guerin, G.; Bishop, K. J.; Winnik, M. A.; Ozin, G. A. J. J. o. t. A. C. S., Polymer-like conformation and growth kinetics of Bi2S3 nanowires. **2012,** *134* (22), 9327-9334.
56. Liu, Q.; Wang, X. J. C. S., Fabricating sub-nanometer materials through cluster assembly. **2022,** *13* (42), 12280-12289.
57. Fu, H.; Xu, Y.; Qiu, D.; Ma, T.; Yue, G.; Zeng, Z.; Song, L.; Wang, S.; Zhang, S.; Du, Y. J. A. C. I. E., A Library of Rare Earth Oxide Ultrathin Nanowires with Polymer‐Like Behaviors. **2022,** *61* (45), e202212251.
58. Gras, P.; Rey, C.; Marsan, O.; Sarda, S.; Combes, C., Synthesis and Characterisation of Hydrated Calcium Pyrophosphate Phases of Biological Interest. *Eur. J. Inorg. Chem.* **2013,** *2013* (34), 5886-5895.
59. Bailey, R. T.; Holt, C., Fourier transform infrared spectroscopy and characterisation of biological calcium phosphates. In *Calcified Tissue*, Hukins, D. W. L., Ed. Macmillan Education UK: London, 1989; pp 93-120.
60. Safronova, T. V.; Putlyaev, V. I.; Kurbatova, S. A.; Shatalova, T. B.; Larionov, D. S.; Kozlov, D. A.; Evdokimov, P. V., Properties of amorphous calcium pyrophosphate powder synthesized via ion exchange for the preparation of bioceramics. *Inorg Mater* **2015,** *51* (11), 1177-1184.
61. Oosterlaken, B. M.; Vena, M. P.; de With, G., In Vitro Mineralization of Collagen. *Adv Mater* **2021,** *33* (16), 2004418.
62. Amjad, Z., Influence of polyelectrolytes on the precipitation of amorphous calcium phosphate. *Colloids Surf.* **1990,** *48*, 95-106.
63. Pourpoint, F.; Diogo, C. C.; Gervais, C.; Bonhomme, C.; Fayon, F.; Dalicieux, S. L.; Gennero, I.; Salles, J. P.; Howes, A. P.; Dupree, R.; Hanna, J. V.; Smith, M. E.; Mauri, F.; Guerrero, G.; Mutin, P. H.; Laurencin, D., High-resolution solid state NMR experiments for the characterization of calcium phosphate biomaterials and biominerals. *J. Mater. Res* **2011,** *26* (18), 2355-2368.
64. Nguyen, C.; Bazin, D.; Daudon, M.; Chatron-Colliet, A.; Hannouche, D.; Bianchi, A.; Côme, D.; So, A.; Busso, N.; Lioté, F.; Ea, H.-K., Revisiting spatial distribution and biochemical composition of calcium-containing crystals in human osteoarthritic articular cartilage. *Arthritis Res. Ther.* **2013,** *15* (5), R103.
65. Wulff, G., XXV. Zur Frage der Geschwindigkeit des Wachsthums und der Auflösung der Krystallflächen. *Z. Für Krist. - Cryst. Mater.* **1901,** *34* (1-6), 449-530.
66. Mai, Y.; Eisenberg, A., Self-assembly of block copolymers. *Chem. Soc. Rev* **2012,** *41* (18), 5969-85.
67. Lu, B. Q.; Garcia, N.; Chevrier, D. M.; Zhang, P.; Raiteri, P.; Gale, J. D.; Gebauer, D., Short-Range Structure of Amorphous Calcium Hydrogen Phosphate. *Cryst. Growth Des.* **2019,** *19* (5), 3030–3038.
68. Shao, C.; Jin, B.; Mu, Z.; Lu, H.; Zhao, Y.; Wu, Z.; Yan, L.; Zhang, Z.; Zhou, Y.;

Pan, H.; Liu, Z.; Tang, R., Repair of tooth enamel by a biomimetic mineralization frontier ensuring epitaxial growth. *Sci. Adv.* **2019,** *5* (8), eaaw9569.
69. Liu, Z.; Shao, C.; Jin, B.; Zhang, Z.; Zhao, Y.; Xu, X.; Tang, R., Crosslinking ionic oligomers as conformable precursors to calcium carbonate. *Nature* **2019,** *574* (7778), 394-398.
70. Zhang, S.; Wang, X., Sub-One-Nanometer Nanomaterials Showing Polymer-Analogue Properties. *ACS Materials Letters* **2020,** *2* (6), 639-643.